Automatic Generation of Boundary Conditions Using Demons Nonrigid Image Registration for Use in 3-D Modality-Independent Elastography

Thomas S. Pheiffer*, Jao J. Ou, Rowena E. Ong, and Michael I. Miga

***Abstract*—Modality-independent elastography (MIE) is a method of elastography that reconstructs the elastic properties of tissue using images acquired under different loading conditions and a biomechanical model. Boundary conditions are a critical input to the algorithm and are often determined by time-consuming point correspondence methods requiring manual user input. This study presents a novel method of automatically generating boundary conditions by nonrigidly registering two image sets with a demons diffusion-based registration algorithm. The use of this method was successfully performed *in silico* using magnetic resonance and X-ray-computed tomography image data with known boundary conditions. These preliminary results produced boundary conditions with an accuracy of up to 80% compared to the known conditions. Demons-based boundary conditions were utilized within a 3-D MIE reconstruction to determine an elasticity contrast ratio between tumor and normal tissue. Two phantom experiments were then conducted to further test the accuracy of the demons boundary conditions and the MIE reconstruction arising from the use of these conditions. Preliminary results show a reasonable characterization of the material properties on this first attempt and a significant improvement in the automation level and viability of the method.**

***Index Terms*—Boundary conditions, elastography, finite element methods, image registration.**

I. Introduction

AN IMAGING methodology that utilizes the mechanical properties of tissue is known as elastography. Elastography employs a combination of image processing and measurements of the physical deformation of the tissue to create a representation of the mechanical strength of structures inside an organ [1], [2]. The overall principle behind elastography for use in cancer imaging is that regional changes in tissue architecture resulting from the manifestation of disease result in detectable changes in mechanical properties. For example, breast cancers have been widely recognized in the medical community as much firmer to the touch than the surrounding soft tissue. The biological basis for this effect is due to changes in tissue composition, such as varied expression of collagen and greater numbers of fibroblasts [3], [4]. The exploitation of a contrast mechanism based on elastic properties may have considerable potential to characterize disease states.

Several kinds of elastography exist, such as ultrasound elastography (USE) and magnetic resonance elastography (MRE) which have already shown promise in diagnosing solid lesions in breast tissue and other physiological locations. The first introduction of USE demonstrated that images from A-line ultrasound could provide axial strain estimates [5]. Elastography has also been applied within the MR imaging domain, whereby motion-sensitized gradient sequences were used to visualize and quantify strain wave propagation in media [6]. A relatively new method known as modality-independent elastography (MIE) has recently shown potential for supplementing other imaging modalities such as MR and CT for detection of solid tumors in soft tissue [7]. MIE has the benefit of being flexible with regard to its inputs, and unlike USE and MRE, it is not reliant on a particular imaging modality. MIE involves imaging a tissue of interest before and after compression, and then applying a finite element (FE) soft-tissue model within a nonlinear optimization framework in order to determine the elastic properties of the tissue. The group of Shi and Liu also has used FE biomechanical models to estimate material properties of the heart using *a priori* information [8]. A requirement of the MIE method is that appropriate boundary conditions be designated for use in the biomechanical model. Generation of accurate boundary conditions is problematic because soft-tissue organs are nonrigid structures, which invalidates the use of standard rigid registration techniques. Techniques that have addressed this issue in the past have required a significant amount of user interaction. The goal of this study is to develop and validate a method of generating boundary conditions automatically by registering organ surfaces before and after mechanical loading. While breast-like phantoms are used as a demonstration of the method, the intention is to make a more broadly applicable method that may be applied to other organs, such as the brain, liver, or lung.

The previous gold standard in generating boundary conditions for MIE has been feature-based registration methods [9]. Conventionally, this entails employing point correspondence methods facilitated by attached fiducials and assisted by thin-plate spline (TPS) interpolation [10] to create boundary conditions that nonrigidly map the predeformed organ surface to the postdeformed organ surface. This registration process requires the

Manuscript received September 24, 2010; revised January 16, 2011 and May 12, 2011; accepted May 16, 2011. Date of publication June 16, 2011; date of current version August 19, 2011. This work was supported by the National Institutes of Health, National Institute for Neurological Disorders and Stroke under Grant R01 NS049251. *Asterisk indicates corresponding author.*

*T. S. Pheiffer is with the Department of Biomedical Engineering, Vanderbilt University, Nashville, TN 37235 USA (e-mail: thomas.s.pheiffer@vanderbilt.edu).

J. J. Ou, R. E. Ong, and M. I. Miga are with the Department of Biomedical Engineering, Vanderbilt University, Nashville, TN 37235 USA (e-mail: jjo@alumni.duke.edu; rowena.ong@vanderbilt.edu; michael.i.miga@vanderbilt.edu).

Digital Object Identifier 10.1109/TBME.2011.2159791

tedious task of applying and subsequently localizing numerous surface markers within the image space, determining point correspondence, creating a TPS interpolation, and finally calculating a set of Dirichlet boundary conditions for use in the MIE method. Initial attempts to reduce the complexity and level of user interaction have focused on the use of two energy minimization techniques [11]. These techniques relied upon partial differential equation (PDE) solutions of Laplace's equation or the diffusion equation, respectively, across the surface of the organ geometry in the pre- and postdeformed states. Like-valued isocontours from the solutions on each surface (i.e., predeformed and postdeformed) act as "virtual" fiducials to assist in correspondence using a symmetric closest point approach [12]. Dirichlet boundary conditions are generated after the assigned correspondence is determined and this completes the required input for the MIE algorithm. Both methodologies required conditions to be manually specified to various regions of the mesh. While the results presented by *Ong et al.* [11] indicated better performance via the Laplacian method, the diffusion method did not require the difficult task of assigning a boundary condition to the chest wall in both pre- and postdeformed mesh domains. These methods, as well as the TPS method, will be compared to the intensity-based approach in this paper.

While the aforementioned PDE-based methods represented an improvement in automation over the TPS method for generating boundary conditions for the MIE algorithm, the ideal boundary condition method would be both fully automated and require no fiducials. There is precedent for using nonrigid image registration to generate boundary conditions for FE tissue volume models, as presented by Tanner *et al*. [13]. There is a wide variety of nonrigid registration algorithms based on intensity, such as the B-spline registrations of [14] or various diffusive flow methods [15], [16]. This study presents an approach for automatically generating boundary conditions through the use of a nonrigid image registration algorithm called demons diffusion. The demons method was chosen based on its popularity and ease of implementation. The demons method was first proposed by Thirion [17] and is well understood to have a strong mathematical foundation as in the works of Pennec *et al*. [18], Cachier *et al*. [19], and Modersitzki [20]. The basic premise presented by Thirion [17] is to use an optical flow model governed by the idea of Maxwell's demons to drive the registration. In this model, the intensity of a moving object is considered to be constant with time, which implies that some level of correspondence can be achieved between deformed and undeformed images, as long as the intensity profiles are very similar. The object boundaries in one image are characterized as semipermeable membranes, and the other image is allowed to diffuse through these membranes based upon the optical flow equation

$$\mathrm{D}(\mathrm{X}) \cdot \nabla \mathrm{f}(\mathrm{X}) = -(\mathrm{m}(\mathrm{X}) - \mathrm{f}(\mathrm{X})) \tag{1}$$

where f(X) is the fixed target image, m(X) is the source image being deformed for the registration, and D(X) is the displacement field mapping the source to the target image through an instantaneous optical flow. Thirion reformulated equation (1) to an algorithmic iterative form as follows:

$$\mathrm{D}^{\mathrm{N}}(\mathrm{X}) = \mathrm{D}^{\mathrm{N}-1}(\mathrm{X}) - \frac{(\mathrm{m}(\mathrm{X} + \mathrm{D}^{\mathrm{N}-1}(\mathrm{X})) - \mathrm{f}(\mathrm{X}))\nabla \mathrm{f}(\mathrm{X})}{\|\nabla \mathrm{f}\|^2 + (\mathrm{m}(\mathrm{X} + \mathrm{D}^{\mathrm{N}-1}(\mathrm{X})) - \mathrm{f}(\mathrm{X}))^2} \tag{2}$$

The displacement field obtained from (2) is smoothed with a Gaussian filter between each iteration in order to regularize the registration. The popularity of the demons algorithm has also helped it remain an active area of research. Vercauteren *et al*. recently introduced symmetric diffeomorphic demons [21]–[23], and improvements to the registration regularization continue to be made by Cahill *et al*. [24], Mansi *et al.* [25], and other groups. In this paper, the demons algorithm was used to perform image matching of pre- and post-deformation images and tested against a controlled *in silico* simulation with known boundary conditions. The generated boundary conditions were also used to perform an MIE elasticity reconstruction to evaluate its effectiveness in determining the elasticity contrast of a previously characterized system. The simulation study was followed by two phantom experiments to further stress the abilities of this new approach.

II. Methodology

A. Automatic Generation of Boundary Conditions

As described in the previous work, the MIE algorithm is comprised of three major components: 1) a biomechanical FE model of soft-tissue deformation based on material properties; 2) a similarity metric with which to compare images; and 3) an optimization routine to update the material properties in the model [26].

The process of generating an elasticity reconstruction begins with the acquisition of an image of the organ. A mechanical load is then applied to the tissue, and the organ is imaged again. These pre- and post-deformation images comprise the primary input to the MIE algorithm and are referred to as the source and target images, respectively. The organ boundary is then segmented manually in the predeformed source image, and its surface geometry is extracted using the marching cubes algorithm, which allows an FE mesh of tetrahedrons to be created from the surface information. The mesh is partitioned into "regions" to which elasticity properties are assigned, which defines the resolution of the elastographic reconstruction. The biomechanical model used for the reconstruction is a linear elastic model, which holds that the strain experienced is proportional to the applied stress. We further assume that the materials of the FE mesh within a given region are isotropic and nearly incompressible in nature. Although tissue is known to have somewhat complex mechanical behavior, the system may be approximated as linear elastic with sufficiently small strains (all strains in this work are less than 15%). In work not presented here, it was found that a Poisson's ratio of 0.485 was optimal for use in MIE, and was used for all of the following experiments. The other critical material property in the model is Young's modulus *E*, which is solved for by the MIE framework. The ability of the biomechanical model to accurately deform the mesh of the candidate tissue volume is dependent on the accuracy of its boundary conditions.

Once boundary conditions have been designated, the model is run and the FEM displacement solution for all the nodes in the mesh is obtained. The displacements are then used to deform the original pre-deformation image, which is then compared with the known post-deformation target image to generate an image similarity measurement. A nonlinear optimization framework is used to update the material properties of the mesh based on the modeled deformation. The optimization is the minimization of the objective function

$$\psi = |S_{\mathrm{TRUE}} - S_{\mathrm{EST}}|^2 \tag{3}$$

where S_{TRUE} is the similarity value achieved when comparing the target image to itself and S_{EST} is the similarity between the target and model-deformed source images. Differentiating (3) with respect to the elasticity distribution and setting the resulting expression equal to zero give a series of nonlinear equations that are solved using the Levenberg–Marquardt method:

$$[J^T J + \alpha I]\{\Delta E\} = [J^T]\{S_{\mathrm{TRUE}} - S_{\mathrm{EST}}\} \tag{4}$$

where J is the Jacobian matrix whose size is determined by the number of material property regions, ΔE is the vector of updates to the material property distribution defined by the regions, and α is an empirical regularization parameter determined by the methods of Joachimowicz *et al.* [27]. Modulus values in the mesh are updated by ΔE until an error tolerance on the relative objective function error evaluation is reached, at which point the reconstructed elastographic image is created from the current distribution of E values in the mesh regions.

The implementation of the demons algorithm used in this study to generate boundary conditions for the aforementioned model was based on the Insight Toolkit [28], [29], and was derived from the original demons registration presented by Thirion. This included the use of simple Gaussian smoothing of the deformation field as the regularization of the registration. It should be noted that there is a multitude of regularization schemes in the literature, including those that imitate linear elasticity [30], or elastic-like vector filters [31], which could potentially improve the results presented here. The two parameters of the registration were the number of iterations (single-resolution registrations) and the standard deviation of the Gaussian smoothing kernel. The number of iterations required was chosen separately for each dataset such that the updates to the deformation field were observed to become very small by the end of the registration. In results not presented here, a brief sensitivity analysis was performed on the sigma value for the registration of the simulations, and it was found that over a range of 0 to 3 voxels for sigma, that 1.5 resulted in the most accurate deformation field. As the smoothing became stronger than 1.5, we noticed that the error became greater around the area of the depressions, as the kernel began to excessively smooth the depression displacements. Therefore, this number was used in all of the reported experiments. When the registration is executed, it produces displacements at the centroid of every voxel. The displacement vectors are then interpolated onto the nodal coordinates of the FE mesh using a cubic 3-D interpolation. The displacements that are assigned to boundary nodes are thus designated as Type-I boundary conditions for the biomechanical model.

B. Simulations

In order to evaluate the demons method of generating boundary conditions for MIE as described earlier, a controlled experiment was conducted by obtaining a CT and an MR image volume of human breast tissue and registering them to target images created by simulated mechanical loads. The two image sets (CT and MR) of normal tumor-free human breast tissue were obtained from the UC-Davis Department of Radiology and the Vanderbilt University Institute of Imaging Science, respectively, for use in this study. The surface of each tissue volume was segmented from the surrounding structures in the images with ANALYZE 8.1 (Mayo Clinic, Rochester, MN) and the resulting segmentation was used to create a 3-D FE mesh using a tetrahedral mesh generation algorithm [32]. For both the CT set and the MR set, a 2-cm spherical tumor was synthetically implanted in the center of the respective mesh and assigned an elasticity value six times higher than the surrounding material, which is consistent with breast cancer elasticity contrasts in the literature [33]. This contrast ratio of 6:1 was thus considered to be the goal for reconstruction in both cases.

Each FE mesh was deformed by applying a depression to one side of the tissue volume. The displacements predicted by the model were then used to deform the CT and MR source images to provide simulated target images. Using the pre- and postdeformed image volumes, the demons registration could be executed and compared to the known displacements responsible for the simulated tissue deformations. In addition, the surface displacements could be used to test the accuracy and fidelity of the 3-D MIE reconstructions conducted with demons-based boundary conditions. The registration for both simulations utilized 2500 iterations with a σ of 1.5 voxels.

C. Phantom Experiment 1

After demonstrating the efficacy of the demons method in this highly controlled *in silico* simulation study, the next step was to apply the same tests to real-world data with realistic amounts of noise and uncertainty. To this end, phantom images were acquired to evaluate the ability of the demons method to produce accurate boundary conditions when compared to the current gold standard method.

As described in [11], the phantom used in this study (hereafter referred to as Phantom 1) was created from an 8% w/v solution of polyvinyl alcohol (Flinn Scientific, Batavia, IL) in an anthropomorphic breast mold. To provide intrinsic fiducial markers, 34 1-mm stainless steel beads were distributed over the phantom directly under its surface. It should be noted that except for the beads, there was little to provide intensity heterogeneity within this phantom. A mechanical load was applied to the phantom in a custom-built acrylic chamber via a neoprene sphygmomanometer air bladder (W.A. Baum, Copiague, NY) positioned on the side of the phantom.

The phantom was subjected to three levels of compression by inflation of the air bladder: no compression, inflation with

50% of the maximum bladder pressure, and full inflation of the bladder. At each state of compression, CT images were acquired with dimensions $512 \times 512 \times 174$ and $0.54 \times 0.54 \times 1$ mm voxel size. The images were then segmented and triangular meshes were created from the surface geometry of the phantom. From the surface meshes, the fiducial bead centroid positions were localized and then used in a TPS interpolation to provide the gold standard boundary conditions for two scenarios: 1) deforming from the uncompressed state to the 50% compression state; and 2) deforming from the uncompressed state to the 100% compression state. In generating the TPS boundary conditions, 33 of the beads were used in calculating the interpolation, while the last fiducial was used to evaluate the target registration error (TRE). In an effort to evaluate the error over the entire surface, the TPS registration was conducted 34 times, each time using a different fiducial for the TRE calculation. The final TRE for the TPS gold standard was the average of these repetitions. The demons method was then used independently to generate boundary conditions mapping from the pre- to the post-deformed surface of the phantom for the two scenarios, and compared to the control TPS result, as well as the previous semiautomated methods (Laplace equation and diffusion methods). The registration in both scenarios utilized 120,000 iterations and σ of 1.5 voxels.

D. Phantom Experiment 2

Following the evaluation of the performance of the demons method in generating boundary conditions in the aforementioned phantom study, a second phantom experiment was designed to test the performance of demons-based boundary conditions in the context of a full MIE reconstruction. Two more phantoms (hereafter referred to as Phantom 2 and Phantom 3) were constructed of polyvinyl alcohol cryogel to test the accuracy of the reconstruction when validated with material testing data. As described by Ou [34], the two new phantoms were created in a manner similar to the first phantom. However, these phantoms each included a 25-mm diameter phantom tumor composed of a stiffer gel than the bulk gel. Barium sulfate was mixed with the tumor gel and was randomly added in streams to the bulk gel to provide contrast for the CT images. Similar to the first phantom study, polytetrafluoroethylene spherical beads (McMaster-Carr, Atlanta, GA) with a 1.6-mm diameter were distributed just under the surface of the phantoms in order to facilitate a TPS interpolation to act as the gold standard boundary conditions. Phantom 2 received 35 beads, while Phantom 3 received 32 beads. The TRE for the TPS registration was calculated as before. To provide validation for MIE reconstructions in Phantoms 2 and 3, independent mechanical tests were performed on samples of the two gel elasticity constituents of the phantom. A sample from each gel (tumor and normal) was set aside for this testing during fabrication. Each was subjected to compression testing using an ElectroForce 3100 material tester (Bose, Eden Prairie, MN). The instrument was programmed to provide fixed displacements to the cryogels when the samples were mounted on a platform over a 22.5 N load cell. Each sample was subjected to five cycles of a load rate of 0.15 mm/s and then held for 300 s for strains of 2%, 5%, 10%, and 15% in compliance with small deformation theory. Average elastic modulus values for the two gels were obtained from the slope of the stress–strain curves of the steady-state loading phases.

The phantoms were imaged in the previously described air bladder chamber using a CT scanner (Philips Medical, Bothell, WA). The Phantom 2 CT images (pre- and post-deformation) were reconstructed with dimensions of $512 \times 512 \times 143$ and voxel spacing of $0.27 \times 0.27 \times 0.8$ mm, while the Phantom 3 CT images were reconstructed with dimensions of $512 \times 512 \times 139$ and voxel spacing of $0.26 \times 0.26 \times 0.8$ mm. The predeformed source image surfaces were then used to create tetrahedral meshes. The Phantom 2 mesh was constructed of 30, 900 nodes and 166,509 elements, while the Phantom 3 mesh was constructed of 33,930 nodes and 183,609 elements. The TPS boundary conditions were generated using the implanted beads as control points for a TPS interpolation between the pre- and post-deformation surfaces for each phantom set. The PDE-based and demons methods were then utilized to independently generate boundary conditions for the two phantoms. The demons registration was set to run for 30,000 iterations with a σ of 1.5 voxels.

The accuracy of the demons-based boundary conditions was evaluated by comparing the gold standard TRE of the TPS method, the TRE of the PDE-based methods, and the TRE of the points when used in the demons method. The appropriateness of demons-based boundary conditions was then tested by employing them in an MIE reconstruction comparing elastic modulus values to independent measurements. To constrain the problem, only two regions of material properties were designated in the mesh: the tumor and the bulk normal gel. *A priori* knowledge of the location of the tumor was also used by segmenting the tumor margins from the normal gel beforehand in order to assign the material types to their corresponding elements in the FE model. The results of the MIE reconstruction using demons-based boundary conditions were also compared to the results of the reconstruction when using TPS boundary conditions and those derived from the PDE methods. Poisson's ratio used in the model for both experiments was 0.485 to approximate an incompressible tissue-mimicking material.

III. Results

A. Simulations

The CT and MR image source images were acquired and then deformed with the set of known boundary conditions as shown in Fig. 1. The deformations applied in both cases were approximately Gaussian in distribution across the depressions. The maximum displacement experienced by the CT set was approximately 13 mm, whereas the maximum experienced by the MR set was approximately 12 mm.

The demons method was then used to register the source images to their respective target images and automatically generate boundary conditions for the source meshes. The TRE calculated from the boundary nodes was then calculated, and is visualized in Fig. 2.

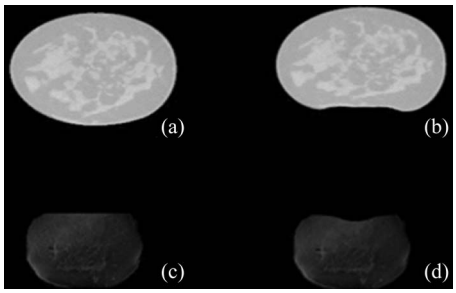

Fig. 1. Representative slices from the two datasets used for the simulations. Slices (a) and (b) show the pre- and postdeformed CT sets, whereas slices (c) and (d) show the pre- and postdeformed MR sets, respectively.

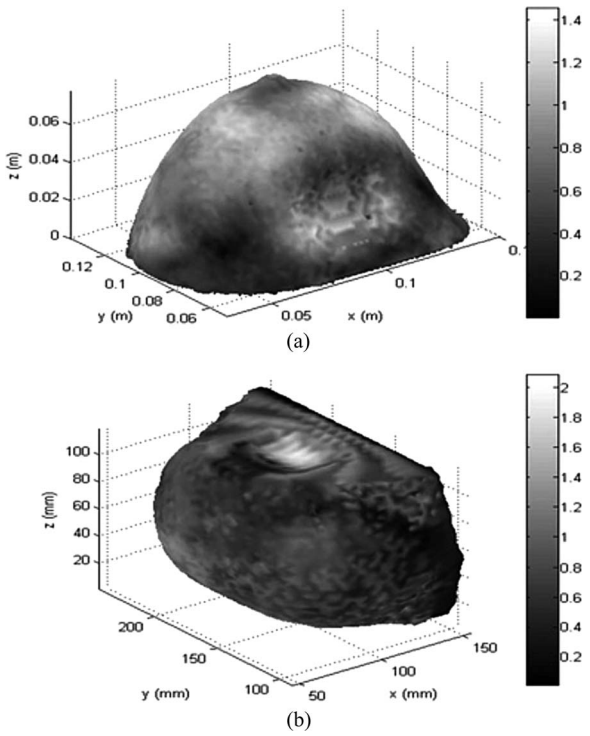

Fig. 2. TRE distribution (in mm) across the surfaces of (a) the CT mesh and (b) the MR mesh for the demons-based boundary conditions compared to the known conditions.

The light surfaces of the mesh correspond to areas that experienced greater error when compared to the known boundary conditions. Averaging over all the nodes on the boundary, the CT set experienced a mean error of 0.6 mm $\pm$0.3 mm with a maximum error of 1.5 mm, which represents an average difference of about 17% between the magnitude of the TRE vectors and the magnitudes of the known displacement vectors. The MR set experienced a mean error of 0.5 mm $\pm$ 0.3 mm with a maximum error of 1.9 mm, which represents a mean difference of about 23%. The demons-based boundary conditions were then utilized in an MIE reconstruction in an attempt to recapture the known 6:1 contrast in the simulations. The tumor-to-normal elasticity contrast calculated by the MIE algorithm was 3.63:1 for the CT set, and was 5.46:1 for the MR set. The results of the boundary condition accuracy and the resulting contrast ratios are shown in Table I, as well as a comparison with the results of the three other boundary condition methods.

Fig. 3 illustrates the relationship between elasticity contrast ratios (tumor-to-normal) and the associated objective function values in the MIE optimization routine. The minima in the objective function space correspond to elasticity contrast values which resulted in an optimally deformed image. Shown in the figure are the objective function values of the deformations using the known boundary conditions (as the control) and the demons boundary conditions.

B. Phantom Experiment 1

In the first phantom experiment, CT images of Phantom 1 were acquired at no compression, 50% compression, and 100% compression and segmented from the compression chamber. The demons method was used to generate Type-I boundary conditions to map from the uncompressed state to the 50% state, and another set of boundary conditions to map from the uncompressed state to the 100% state. The implanted beads on the surface of the phantom were used to calculate the TRE of this surface registration in both cases. The average TRE for 50% compression when using the demons boundary conditions was approximately 3.3 mm $\pm$1.32 mm, with a maximum TRE of 6.1 mm. The average TRE for 100% compression was approximately 6.8 mm $\pm$3.2 mm, which a maximum of 14.2 mm. The Phantom 1 results are directly compared in Table II to the gold standard TPS result and the results of the previous semi-automated methods, as well as to analogous results from Phantom 2 and Phantom 3.

C. Phantom Experiment 2

In the second phantom experiment, CT images of Phantom 2 and Phantom 3 were acquired and segmented from the compression chamber for pre- and post-depression. Phantom 2 is shown in Fig. 4 as an example. The embedded tumor in Phantom 2 was about 12 mm from the surface. The tumor in Phantom 3 was located further from the site of depression, at about 26 mm from the surface. Qualitatively, the streams of barium sulfate which were distributed throughout the gel provided an increase in the image texture of these phantom images over the Phantom 1 images, which lacked this texture enhancement.

The demons method was applied to both phantoms to acquire Type-I boundary conditions for each mesh. The TRE of the demons-based conditions was evaluated by comparing to the known point correspondence of the implanted surface beads. The average demons-based TRE for Phantom 2 was calculated to be approximately 1.6 mm $\pm$1.0 mm, with a maximum experienced TRE of 4.9 mm. For Phantom 3, the average TRE was 1.9 mm $\pm$1.2 mm, with a maximum TRE of 4.3 mm. These values are directly compared in Table II to the performance of the gold standard TPS interpolation method and two previous semiautomated methods, as well as the Phantom 1 results. As the results showed that the PDE-based methods were not notably more accurate for Phantoms 2 and 3 than the TPS or demons methods, only the demons method and TPS method were used in MIE reconstructions for comparison. The material testing data

TABLE I
COMPARISON OF BOUNDARY CONDITION MAPPING ERROR AND MIE RECONSTRUCTION RESULTS BETWEEN THE FOUR METHODS FOR THE SIMULATIONS

	Boundary Condition Mapping Error		MIE Reconstruction Results (x:1)	
	CT Mean TRE (max) mm	MR Mean TRE (max) mm	CT Elasticity Contrast Ratio	MR Elasticity Contrast Ratio
TPS (40 pts.)*	0.30 (2.6) *	0.033 (0.6)*	5.66**	6.26**
Laplace*	0.53 (2.6)*	0.48 (2.5)*	5.02**	673**
Diffusion*	1.5 (8)*	0.61 (2.9)*	17.5**	348**
Demons	0 60 (1.5)	0.50 (1.9)	3.63	5.46

* [11].
**[9].

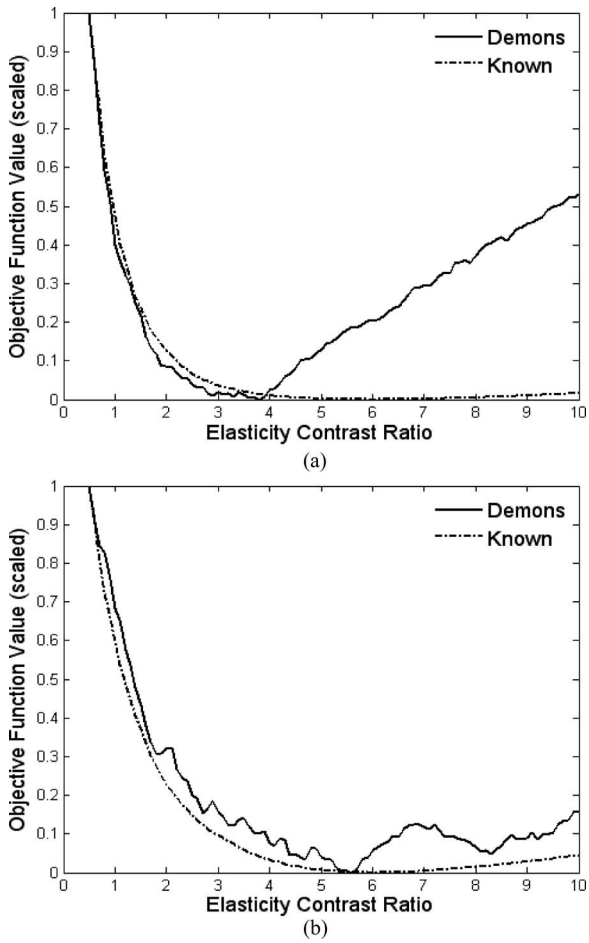

Fig. 3. Objective function maps for (a) the CT simulation and (b) the MR simulation. The objective function value calculated by the optimization framework is plotted on the ordinate axis against selected elasticity contrast ratios (tumor-to-normal) as affected by the boundary conditions. Shown are the objective maps of the demons case (solid lines) and the known boundary conditions as the control (dashed lines). The ordinate is scaled in both cases.

resulted in an average contrast ratio of 4.10:1 for the gels. The demons-based boundary conditions were then used in an MIE reconstruction for each phantom. The tumor-to-normal elasticity contrast for Phantom 2 was calculated by the MIE algorithm to be 4.70:1.

The elasticity contrast for Phantom 3 was calculated to be 2.46:1. In Table III, these values are compared to the contrast ratios that were calculated by MIE using the gold standard TPS boundary conditions, and to the material testing data as validation for the accuracy of the MIE method.

Fig. 5 illustrates the relationship between elasticity contrast ratios (tumor-to-normal) and the associated objective function values in the MIE optimization routine. Shown in the figure are the objective function values of the deformations using the TPS boundary conditions (as the control) and the demons boundary conditions.

IV. DISCUSSION

A. Simulations

The demons-based boundary conditions resulted in deformed meshes for the simulation experiment which were qualitatively very close in appearance to the known target meshes for both the CT and MR datasets. Quantitatively, the average difference between the demons conditions and the known conditions was about 20% for both sets, which was an encouraging indication of the ability of the demons methods to automatically provide boundary conditions that would have adequate accuracy for use in MIE. In Fig. 2, it can be seen that the largest errors were spread across the regions of high curvature around the tip of the tissue volume and in the dip of the artificial depression for the CT set, while in the MR set the errors were mostly localized to the depression area.

The accuracy of the demons-based boundary conditions for the simulations was compared to the results of past methods in Table I. Unsurprisingly, the TPS method remained the most accurate of the four methods when considering the average boundary condition error. The demons method performed about as well as the Laplace method, and clearly outperformed the diffusion method for the CT set in terms of the average error. However, the demons method performed favorably compared to all of the other methods in terms of maximum TRE for that set, as its maximum error was well below those of the other methods. In terms of average surface TRE, the demons method was also comparable to the PDE-based method for the MR set as well. However, with the exception of the TPS method, the demons boundary conditions again compared favorably against the other methods in terms of the maximum error experienced on the boundary.

The results of the boundary condition accuracy experiment were encouraging and indicated that demons-based boundary conditions were a feasible solution to the MIE boundary condition problem. The results of the MIE reconstruction for the CT and MR simulation sets were shown in Table I and compared to the results of reconstructions that utilized boundary

TABLE II
COMPARISON OF BOUNDARY CONDITION MAPPING ERROR BETWEEN THE FOUR METHODS FOR THE TWO PHANTOM EXPERIMENTS

	Boundary Condition Mapping Error			
	Phantom 1		Phantom 2	Phantom 3
	50% Compression Mean TRE (max) mm	100% Compression Mean TRE (max) mm	Single Compression Mean TRE (max) mm	Single Compression Mean TRE (max) mm
TPS	1.1 (3.4)*	1.7 (5.1)*	1.4 (7.08)**	1.24 (4.9)**
Laplace	3.4 (8.6)*	6.3 (15.3)*	4.22 (7.26)	2.24 (4.74)
Diffusion	2.7 (6.9)*	5.7 (13.6)*	4.11 (6.57)	2.35 (6.36)
Demons	3.3 (6.1)	6.8 (14.2)	1.55 (4.92)	1.85 (4.34)

*[11].
**Based on work in [34].

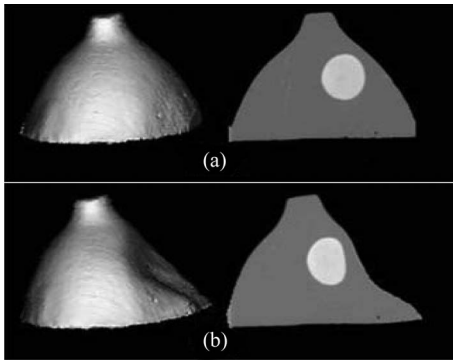

Fig. 4. Representative (a) source and (b) target geometry of the anthropomorphic phantoms, with center slices. Phantom tumors as shown here were present in Phantoms 2 and 3 only.

TABLE III
MIE-RECONSTRUCTED ELASTICITY CONTRAST RATIOS FOR PHANTOMS 2 AND 3 AND GEL MATERIAL TESTING DATA

	Phantom 2 Reconstructed Contrast Ratio	Phantom 3 Reconstructed Contrast Ratio	Material Tester Contrast Ratio*
TPS*	3.81	3.06	4.10
Demons	4.70	2.46	

*[9].

conditions generated from the other three methods. Unsurprisingly, the table shows that the TPS boundary conditions, which were the most accurate of the four, resulted in elasticity contrast ratios for both sets that were closer to the known ratio of 6:1 than any of the other boundary conditions. For the application of the demons registration-based boundary conditions to the CT dataset, the elasticity reconstruction with spatial *a priori* knowledge of the tumor converged to a contrast ratio of 3.63:1. Similarly, the MR data resulted in a contrast ratio of 5.46:1. Compared to the known designated material contrast of 6:1, there is clearly a discrepancy in these reconstruction behaviors that needs to be investigated. The difference, particularly between the different modalities of input data, is likely due to a combination of factors including mesh geometry and image quality. In addition, the distance of the tumor from the area of greatest displacement likely affects the accuracy of the reconstruction since the displacements of nodes are expected to decrease the further they are located away from the depression. These simulations did not investigate the effect of tumor distance on the reconstruction. Notably, the diffusion method resulted in a much higher contrast ratio for the CT set than the demons method, while the Laplace method resulted in a contrast ratio that was closer to 6:1 but was an underestimation rather than an overestimation of the true value. The ability of the demons-based conditions to provide a contrast that was more accurate than the diffusion method for the CT simulation was encouraging. Even more suggestive was the behavior of the MR reconstruction. The Laplace and diffusion boundary conditions introduced instabilities into the MIE algorithm, which resulted in contrast estimates that were unreasonably higher than the true value. The demons-based conditions allowed the algorithm to provide a contrast estimate that was closer to the known value.

Introducing the inexact demons boundary conditions to the model had a noticeable effect on the objective function profile, as shown in Fig. 3, by shifting the minimum objective function value to a different optimal elastic contrast ratio for both the CT and the MR simulation. The shift was much more pronounced for the CT simulation, for which the new optimal objective function value corresponded to a contrast ratio of about 3.80:1 instead of 6:1 as predicted by the known boundary conditions. Additionally, the convexity of the function was altered significantly, with very little variation in the objective function for contrast ratios in the immediate vicinity of the global minimum. The MR simulation also experienced a shift in the optimal objective function when demons boundary conditions were used instead of the known conditions, with a new optimal contrast of about 5.50:1. This represented only a slight decrease from the desired 6:1 prediction. The objective function values arise from the image similarity metric, which again suggests that the difference in objective maps between the two simulations is influenced by the image texture characteristics. It is also clear that the addition of inaccuracies within the boundary conditions alters the nature of the objective function by injecting local minima and undesirable variations, which may necessitate a filtering approach to ensure global minima are found.

B. Phantom Experiment 1

While the efficacy of the automated demons method was shown by the simulations to be comparable to the semi-automated Laplace method and somewhat better than the

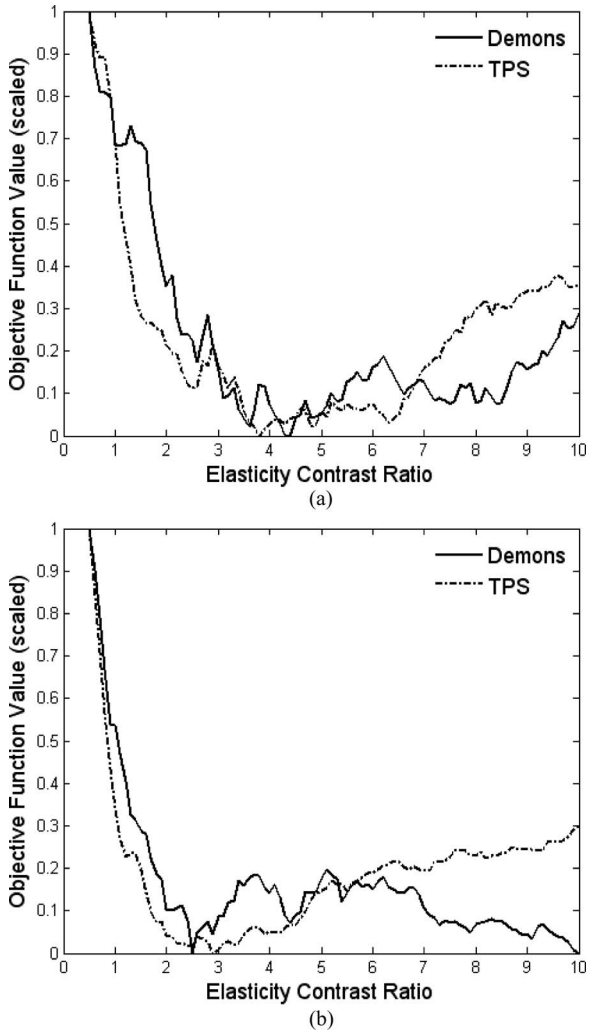

Fig. 5. Objective function maps for (a) Phantom 2 and (b) Phantom 3. The objective function value calculated by the optimization framework is plotted on the ordinate axis against selected elasticity contrast ratios (tumor-to-normal) as affected by the boundary conditions. Shown are the objective maps of the demons case (solid lines) and the known boundary conditions as the control (dashed lines). The ordinate is scaled in both cases.

diffusion method, the simulations were in several ways performed under optimal conditions. The image volumes qualitatively had a great deal of heterogeneity and texture on which the demons registration could act, and with which the MIE optimization routine could use to help accurately update material property assignments. There was also an absolute truth with which to compare, in the form of known boundary conditions. The first phantom experiment sought to provide additional challenge to the demons method in its ability to generate reasonably accurate boundary conditions.

In the first phantom experiment, the results of the demons method were compared to the results of the three other methods in Table II for the two compression states applied to Phantom 1. The table shows that the demons algorithm performed about as well in relation to the other PDE methods as it did in the simulation experiment. Note that Phantom 1 had very little image heterogeneity and would indicate that with a lack of image intensity contrast that the demons-based registration is at least no worse than that achieved by the PDE methods. The gold standard TPS method gave the lowest error. As seen in Table II, the errors given by all of the methods increased when a larger deformation was applied to Phantom 1. The demons boundary conditions became slightly worse in relation to the other methods at the increased level of compression, which suggests that the number of iterations used by the demons algorithm may need to be increased to accommodate larger differences between pre- and post-deformation images, or that the algorithm may be somewhat more sensitive to the lack of image intensity heterogeneity.

In moving from simulation data to "real-world" phantom data, the errors experienced by all four of the methods increased significantly. The Phantom 1 image data were different from the simulation data in several key respects. For example, the target image volume of Phantom 1 represents a completely new acquisition, whereas in the simulation work, postdeformed image sets were generated from the predeformed set. This discrepancy in target image acquisition introduces some uncertainty to the determination of source-to-target correspondence. Another major change from the simulation experiment was the markedly smaller presence of texture in the images due to the homogeneity of the gel. More specifically, the TRE performance varied among the Phantom 1, Phantoms 2 and 3, and simulation results which are listed, respectively, in terms of increasing image texture. Qualitatively observing the results across Tables I and II, the trend of decreasing TRE with increasing texture for the demons-based approach can be observed.

C. Phantom Experiment 2

It was shown in the first phantom experiment that the demons method could produce reasonably accurate boundary conditions compared to the semiautomated Laplace and diffusion methods. The second phantom experiment introduced another set of real-world data, but the images from this experiment had more texture in the form of barium sulfate as a contrast agent, which was intended to allow the demons registration to provide more accurate boundary conditions as needed by the MIE algorithm. In addition, the presence of the stiff tumor allowed for a test of the MIE algorithm's ability to distinguish elasticity contrast in a phantom while using demons-based boundary conditions. This experiment was thus the first in which demons-based boundary conditions were used in an MIE reconstruction for which the true boundary conditions were not absolutely known.

The surface errors calculated from the fiducial point correspondence for the TPS, Laplace, diffusion, and demons methods were compared in Table II for Phantom 2 and Phantom 3. Unsurprisingly, the TPS method performed better with respect to mean accuracy. Notably, the maximum error experienced by the demons method was less than that of the TPS method, which was similar to the result of the CT simulation study. The two PDE-based methods presented error which was similar in scope to their Phantom 1 results. Overall, the demons method performed considerably better on these two phantom sets than it did on Phantom 1, and notably outperformed the Laplacian and diffusion methods. This is most likely due to the increase in

image texture which can be qualitatively observed from visual inspection of the images. Given that clinical images tend to have even more image texture and geometric heterogeneity than found in these phantom images, further investigation into the efficacy of the demons method seems merited.

The utilization of the demons boundary conditions in MIE reconstructions in the second phantom experiment successfully resulted in realistic tumor-to-normal modulus contrast ratios for both phantoms. Due to the observation that the demons method resulted in boundary conditions with comparable (and sometimes superior) accuracy to the Laplace and diffusion methods, only the TPS and demons boundary conditions were utilized in these reconstructions. The results for the TPS- and demons-based MIE reconstructions were compared to each other in Table III as well as to the material tester results. As the table shows, the elasticity contrast ratios for each phantom when using TPS boundary conditions were reconstructed to values with 14–40% difference from the material testing data average. The reconstructions using demons boundary conditions resulted in contrast ratios which were very similar to those of the TPS-based reconstructions, with only a slight drop in contrast. This suggests that the demons boundary conditions were sufficiently accurate for the MIE algorithm to provide a reasonable estimate of the actual gel contrast.

Compared to the control TPS boundary conditions, the demons conditions had a noticeable effect by shifting the minimum objective function value to a different optimal elastic contrast ratio for both phantoms, as shown in Fig. 4. Additionally, the convexity of the function was altered slightly for each. The global minimum of the Phantom 2 objective function was located at an approximate contrast ratio of 4.20:1, which was more similar to the material testing average of 4.10:1 than the case in which TPS boundary conditions were used. The actual contrast ratio to which the MIE reconstruction converged was 4.70:1, which was located on the slope of a local minimum. This behavior was most likely a result of the regularization parameters used in the Levenberg–Marquardt optimization. In the case of Phantom 3, the global minimum was about 2.50:1, which was the approximate value to which the algorithm converged. In this case, the global minimum decreased slightly when using demons instead of TPS conditions.

Observations of Figs. 3 and 5 indicate the change in algorithm performance with respect to simulation and physical data. While the nature of a simulation-to-real transition may be responsible for the increased error in reconstruction, there are several other likely factors involved. Overconstraint of the problem is a possible candidate with the incorporation of the spatial prior. The MIE method works by sampling similarity regionally, i.e., the method breaks up evaluation into many similarity zones (usually over 100) distributed spatially over the domain. The method tries to improve the similarity among all the zones with the use of only two parameters in this case (the elasticity of the background and tumor). This constraint within this type of problem can lead to this type of oscillatory behavior. Another possible reason is the inaccuracy in boundary condition determination due to the dramatic difference in image heterogeneity between simulation and real data. This is supported by the change in TRE. Related to this, it is interesting to note the difference between CT and MR reconstruction for the simulation work associated with Fig. 3 and in light of Table I. The first observation can be made by comparing the control objective function map across CT and MR simulation sets in Fig. 3. Both simulation sets had a contrast ratio of 6:1, with the only difference being the level of intensity heterogeneity, and potential different tissue-volume/tumor geometries/locations. The CT control had a shallower minimum which may affect the reconstruction. When adding to this observation, the objective function maps associated with the demon-based boundary condition it would seem that the CT reconstruction may perform better due to its convexity; but when observing how the minimum has been shifted, and the shape of the control that has no error in boundary conditions, it can be seen that in fact the MR demons-based objective function maps more closely to its control which is reflected in the elasticity contrast ratio.

V. Conclusion

The simulations and phantom experiments conducted in this study indicate that while TPS interpolation remains the most accurate method used, thus far in MIE for generating boundary conditions, the demons method shows promise in situations where fiducial point correspondence data may not be available. In addition, when transitioning from simulation to real data, the discrepancy in performance between TPS and the demons-based boundary condition mapping becomes less (at least in cases where image intensity contrast within the domain is available). Furthermore, while the higher accuracy of the TPS method is desirable, the much higher level of manual user interaction and numerous fiducials needed for the method make clear the desire for alternative methods of boundary condition generation. The demons method proposed represents a fully automated approach.

While the results are encouraging, the challenge of predicting (prior to workflow initiation) how well a pre–post-deformation image set will fare prior to execution of the demons registration and MIE optimization routine still remains. Since the demons registration algorithm possesses diffusive behavior based upon intensity contours as described in [17], it is obvious that the images require a certain level of texture and intensity heterogeneity in order to provide these membranes a meaningful registration. This is one of the likely causes of the varying performance of the demons method in generating accurate boundary conditions among the experiments presented in this paper. In work not presented here, our group observed similar error performance when using a more recent diffeomorphic log-domain version of the demons registration algorithm. While the registration error was virtually the same as the original demons implementation, it is possible that with noisier images, the diffeomorphic nature of the more recent demons may help minimize phenomena such as collapsed mesh elements due to overlapping displacements. Development of a feasibility metric which can predict the success of applying the MIE algorithm to a given image set is a needed next step for the project.

In addition to a threshold criterion to evaluate the potential for a successful reconstruction, the need to generate more realistic phantoms with controllable stiffness properties is also necessary. The breast has a complex image signature even within CT and the reproduction of those patterns coupled with controllable elasticity properties is very challenging. While obstacles remain, the results presented here demonstrate the potential of treating elastographic reconstructions using nonrigid image registration approaches and that the possibility of full automation is also within reach.

ACKNOWLEDGMENT

The authors would like to thank the Vanderbilt Medical Center CT Department for Imaging the Phantoms, as well as Dr. T. Yankeelov and Dr. J. Boone (Department of Radiology, University of California-Davis Medical Center, Sacramento) for the human breast MR and CT datasets, respectively.

REFERENCES

[1] M. Bilgen, "Target detectability in acoustic elastography," *IEEE Trans. Ultrason., Ferroelectr., Freq. Control*, vol. 46, no. 5, pp. 1128–1133, Sep. 1999.

[2] M. M. Doyley, P. M. Meaney, and J. C. Bamber, "Evaluation of an iterative reconstruction method for quantitative elastography," *Phys. Med. Biol.*, vol. 45, no. 6, pp. 1521–1540, 2000.

[3] N. Burns-Cox, N. C. Avery, J. C. Gingell, and A. J. Bailey, "Changes in collagen metabolism in prostate cancer: a host response that may alter progression," *J. Urol.*, vol. 166, no. 5, pp. 1698–1701, 2001.

[4] H. Lee, K. L. Sodek, Q. Hwang, T. J. Brown, M. Ringuette, and J. Sodek, "Phagocytosis of collagen by fibroblasts and invasive cancer cells is mediated by MT1-MMP," *Biochem. Soc. Trans.*, vol. 35, no. Pt 4, pp. 704–706, 2007.

[5] J. Ophir, I. Cespedes, H. Ponnekanti, Y. Yazdi, and X. Li, "Elastography: A quantitative method for imaging the elasticity of biological tissues," *Ultrason. Imaging*, vol. 13, no. 2, pp. 111–134, 1991.

[6] R. Muthupillai, D. J. Lomas, P. J. Rossman, J. F. Greenleaf, A. Manduca, and R. L. Ehman, "Magnetic resonance elastography by direct visualization of propagating acoustic strain waves," *Science*, vol. 269, no. 5232, pp. 1854–1857, 1995.

[7] M. I. Miga, "A new approach to elastography using mutual information and finite elements," *Phys. Med. Biol.*, vol. 48, no. 4, pp. 467–480, 2003.

[8] P. Shi and H. Liu, "Stochastic finite element framework for simultaneous estimation of cardiac kinematic functions and material parameters," *Med. Image Anal.*, vol. 7, no. 4, pp. 445–464, 2003.

[9] J. J. Ou, R. E. Ong, T. E. Yankeelov, and M. I. Miga, "Evaluation of 3D modality-independent elastography for breast imaging: A simulation study," *Phys. Med. Biol.*, vol. 53, no. 1, pp. 147–163, 2008.

[10] A. Goshtasby, "Registration of images with geometric distortions," *IEEE Trans. Geosci. Remote Sens.*, vol. 26, no. 1, pp. 60–64, Jan. 1988.

[11] R. E. Ong, J. J. Ou, and M. I. Miga, "Non-rigid registration of breast surfaces using the laplace and diffusion equations," *Biomed. Eng. Online*, vol. 9, no. 1, pp. 1–14, 2010.

[12] X. Papademetris, A. J. Sinusas, D. P. Dione, R. T. Constable, and J. S. Duncan, "Estimation of 3-D left ventricular deformation from medical images using biomechanical models," *IEEE Trans. Med. Imag.*, vol. 21, no. 7, pp. 786–800, Jul. 2002.

[13] C. Tanner, J. A. Schnabel, D. L. Hill, D. J. Hawkes, M. O. Leach, and D. R. Hose, "Factors influencing the accuracy of biomechanical breast models," *Med. Phys.*, vol. 33, no. 6, pp. 1758–1769, 2006.

[14] D. Rueckert, L. I. Sonoda, C. Hayes, D. L. G. Hill, M. O. Leach, and D. J. Hawkes, "Nonrigid registration using free-form deformations: Application to breast MR images," *IEEE Trans. Med. Imag.*, vol. 18, no. 8, pp. 712–721, Aug. 1999.

[15] W. R. Crum, C. Tanner, and D. J. Hawkes, "Anisotropic multi-scale fluid registration: Evaluation in magnetic resonance breast imaging," *Phys. Med. Biol.*, vol. 50, no. 21, pp. 5153–5174, 2005.

[16] M. S. Froh, D. C. Barber, K. K. Brock, D. B. Plewes, and A. L. Martel, "Piecewise-quadrilateral registration by optical flow—Applications in contrast-enhanced MR imaging of the breast," *Med. Image Comput. Comput. Assist. Interv.*, vol. 9, no. Pt 2, pp. 686–693, 2006.

[17] J. P. Thirion, "Image matching as a diffusion process: An analogy with Maxwell's demons," *Med. Image Anal.*, vol. 2, no. 3, pp. 243–260, 1998.

[18] X. Pennec, P. Cachier, and N. Ayache, "Understanding the 'Demon's Algorithm': 3D Non-Rigid Registration by Gradient Descent," in *Proc. Med. Image Comput. Comput.-Assisted Intervention Conf.*, 1999, pp. 597–606.

[19] P. Cachier, E. Bardinet, D. Dormont, X. Pennec, and N. Ayache, "Iconic feature based nonrigid registration: The PASHA algorithm," *Comput. Vision Image Understanding*, vol. 89, no. 2-3, pp. 272–298, 2003.

[20] J. Modersitzki, *Numerical Methods for Image Registration* (Numerical Mathematics and Scientific Computation). Oxford, U.K.: Oxford Univ. Press, 2004, p. 199.

[21] T. Vercauteren, X. Pennec, A. Perchant, and N. Ayache, "Non-parametric diffeomorphic image registration with the demons algorithm," *Med. Image Comput. Comput. Assist. Interv.*, vol. 10, no. Pt 2, pp. 319–326, 2007.

[22] T. Vercauteren, X. Pennec, A. Perchant, and N. Ayache, "Symmetric log-domain diffeomorphic Registration: a demons-based approach," *Med. Image Comput. Comput. Assist. Interv.*, vol. 11, no. Pt 1, pp. 754–761, 2008.

[23] T. Vercauteren, X. Pennec, A. Perchant, and N. Ayache, "Diffeomorphic demons: Efficient non-parametric image registration," *Neuroimage*, vol. 45, no. 1, pp. S61–S72, 2009.

[24] N. D. Cahill, J. A. Noble, and D. J. Hawkes, "A Demons algorithm for image registration with locally adaptive regularization," *Med. Image Comput. Comput. Assist. Interv.*, vol. 12, no. Pt 1, pp. 574–581, 2009.

[25] T. Mansi, X. Pennec, M. Sermesant, H. Delingette, and N. Ayache, "LogDemons revisited: Consistent regularisation and incompressibility constraint for soft tissue tracking in medical images," *Med. Image Comput. Comput. Assist. Interv.*, vol. 13, no. Pt 2, pp. 652–659, 2010.

[26] M. I. Miga, M. P. Rothney, and J. J. Ou, "Modality independent elastography (MIE): Potential applications in dermoscopy," *Med. Phys.*, vol. 32, no. 5, pp. 1308–1320, 2005.

[27] N. Joachimowicz, C. Pichot, and J. P. Hugonin, "Inverse scattering: An iterative numerical-method for electromagnetic imaging," *IEEE Trans. Antennas Propag.*, vol. 39, no. 12, pp. 1742–1752, Dec. 1991.

[28] T. S. Yoo, M. J. Ackerman, W. E. Lorensen, W. Schroeder, V. Chalana, S. Aylward, D. Metaxas, and R. Whitaker, "Engineering and algorithm design for an image processing Api: A technical report on ITK—The Insight Toolkit," *Stud. Health Technol. Inform.*, vol. 85, pp. 586–592, 2002.

[29] L. Ibanez, W. Schroeder, L. Ng, and J. Cates, *The ITK Software Guide*, 2nd ed. Clifton Park, NY: Kitware, Inc., 2005.

[30] C. Broit, *Optimal Registration of Deformed Images*. Philadelphia, PA: Graduate School Arts Sci., Univ. Pennsylvania, 1981, p. vi, 151l.

[31] P. Cachier and N. Ayache, "Isotropic energies, filters and splines for vector field regularization," *J. Math. Imaging Vision*, vol. 20, no. 3, pp. 251–265, 2004.

[32] J. M. Sullivan, G. Charron, and K. D. Paulsen, "A three-dimensional mesh generator for arbitrary multiple material domains," *Finite Elements in Anal. Design*, vol. 25, no. 3/4, pp. 219–241, 1997.

[33] T. A. Krouskop, T. M. Wheeler, F. Kallel, B. S. Garra, and T. Hall, "Elastic moduli of breast and prostate tissues under compression," *Ultrason. Imaging*, vol. 20, no. 4, pp. 260–274, 1998.

[34] J. J. Ou, "Development of modality-independent elastography as a method of breast cancer detection,", Ph.D. dissertation, Dept. Biomed. Eng., Vanderbilt Univ., Nashville, TN, 2008.

Authors' photographs and biographies not available at the time of publication.